Magnetic topologies of two weak-line T Tauri stars TAP 4 and TAP 40

Yue Xiang, Shenghong Gu, J-F Donati, G Hussain, a Collier Cameron, The Mat y S S E Collaboration

Monthly Notices of the ROYAL ASTRONOMICAL SOCIETY

MNRAS **520,** 3964–3973 (2023) https://doi.org/10.1093/mnras/stad363
Advance Access publication 2023 February 2

Magnetic topologies of two weak-line T Tauri stars TAP 4 and TAP 40

Yue Xiang [1,2★] Shenghong Gu,[1,2,3★] J.-F. Donati [4] G. A. J. Hussain,[5] A. Collier Cameron [6] and the MaTYSSE collaboration

[1] *Yunnan Observatories, Chinese Academy of Sciences, Kunming 650216, China*
[2] *Key Laboratory for the Structure and Evolution of Celestial Objects, Chinese Academy of Sciences, Kunming 650216, China*
[3] *School of Astronomy and Space Science, University of Chinese Academy of Sciences, Beijing 101408, China*
[4] *IRAP, Université de Toulouse, CNRS, UPS, CNES, F-31400 Toulouse, France*
[5] *Science Division, European Space Research and Technology Centre (ESA/ESTEC), Keplerlaan 1, NL-2201 AZ Noordwijk, the Netherlands*
[6] *School of Physics and Astronomy, University of St Andrews, Fife KY16 9SS, UK*

Accepted 2023 January 27. in original form 2022 December 30

ABSTRACT

We present a Zeeman–Doppler imaging study of two weak-line T Tauri stars TAP 4 and TAP 40, based on the high-resolution spectropolarimetric observations with ESPaDOnS at the Canada–France–Hawaii Telescope in November 2013, in the framework of the Magnetic Topologies of Young Stars and Survival of close-in giant Exoplanets large programme. We apply two Zeeman–Doppler imaging codes to the Stokes I and V profiles to reconstruct their brightness and large-scale magnetic field images. The results given by the two imaging codes are in good agreement with each other. TAP 4 shows a large polar cool spot and several intermediate-latitude warm spots on its surface, whereas TAP 40 exhibits very weak variations in its Stokes I profiles, suggesting a mostly unspotted photosphere. We detect Zeeman signatures in the Stokes V profiles of both stars. The reconstructed magnetic maps reveal dominantly toroidal fields, which enclose about 60 per cent of the total magnetic energy for both TAP 4 and TAP 40. Both stars show prominent circular ring features of the azimuthal magnetic field. We derive a solar-like surface differential rotation on TAP 4 from the tomographic modelling. The brightness image of TAP 4 is used to predict the radial velocity (RV) jitters induced by its activity. After filtering out the activity jitter, the rms of its RVs is reduced from 1.7 to 0.2 km s^{-1}, but we do not detect any periodic signals in the filtered RVs of TAP 4, implying that it is unlikely to host a close-in exoplanet more massive than $\sim 3.5 M_{\rm Jup}$ at 0.1 au.

Key words: techniques: polarimetric – stars: imaging – stars: magnetic fields – stars: individual: TAP 4 – stars: individual: TAP 40.

1 INTRODUCTION

Magnetic fields are believed to play a significant role in the formation and evolution of stars and their surrounding planets. Pre-main-sequence (PMS) cool stars show high levels of magnetic activity due to their high rotation rates. Such low-mass stars preserve a high-angular momentum content and they will gradually dissipate it due to magnetic braking. The magnetic field also affects the accretion process of the PMS stars (see Donati & Landstreet 2009, and the references therein).

Zeeman–Doppler imaging, which was first proposed by Semel (1989), takes advantage of a series of time-resolved polarized spectra to recover the magnetic field structure on the stellar surface. It is a powerful tool for the investigation on the properties of magnetic field of young fast-rotating stars at different evolutionary phases, which is important for understanding the evolution of the stellar magnetic field. Magnetic field topologies of Sun-like stars at different evolutionary stages are revealed through Zeeman–Doppler imaging (e.g. Hackman et al. 2016; Hussain et al. 2016; Rosén et al. 2016), but the numbers of systems studied have remained limited up to now.

The Magnetic Topologies of Young Stars and Survival of close-in giant Exoplanets (MaTYSSE) large programme aims to monitor the magnetic field of the young T Tauri stars and search for the potential close-in hot Jupiters (hJs) around them, using the high-resolution spectropolarimetric observations with multiple telescopes (Donati et al. 2014) and Zeeman–Doppler imaging. Through this project, the large-scale magnetic field topologies of a set of young active stars have been recovered (e.g. Donati et al. 2015, 2019; Hill et al. 2017), and the hJs surrounding two very young stars, V830 Tau (Donati et al. 2016) and TAP 26 (Yu et al. 2017), have been detected to date, which have a significant impact on the study of planet formation.

The weak-line T Tauri stars (wTTSs) are young low-mass stars whose inner discs are already dispersed, which is one of the main differences with respect to their progenitors, the classical T Tauri stars. TAP 4 and TAP 40 are two active young wTTSs in Taurus-Auriga (Basri, Martin & Bertout 1991; Grankin et al. 2008). Previous analysis of photometric data indicates that TAP 4 has a short rotational period of 0.482 d and TAP 40 rotates more slowly with a rotational period of 1.555 d (Grankin et al. 2008; Grankin 2013).

★ E-mail: xy@ynao.ac.cn (YX); shenghonggu@ynao.ac.cn (SG)

In this work, we present tomographic modelling of TAP 4 and TAP 40, using two different Zeeman–Doppler imaging codes. We describe the spectropolarimetric observations and data reduction in Section 2, and discuss the evolutionary status and parameters of two stars in Section 3. The tomographic modelling for two stars is conducted in Section 4, including the brightness and magnetic field reconstructions, the surface differential rotation determination, and the radial velocity (RV) filtering. We finally discuss and summarize the results in Section 5.

2 OBSERVATIONS AND DATA REDUCTION

The high-resolution spectropolarimetric observations of TAP 4 and TAP 40 were carried out in November 2013 using the spectropolarimeter ESPaDOnS mounted on the 3.6-m Canada–France–Hawaii Telescope (CFHT). ESPaDOnS has a spectral resolving power of 65 000 and a wavelength coverage from 370 to 1000 nm in spectropolarimeter mode. A total of 31 Stokes I and Stokes V spectra of TAP 4 and 18 spectra of TAP 40 were collected from November 15 to 26, which covered about 23 and 7 rotational cycles of TAP 4 and TAP 40, respectively. We typically obtained 2–4 spectra per night for TAP 4 and 1–2 spectra per night for TAP 40. We summarize the observations, including the UT date, barycentric Julian Date (BJD), peak signal-to-noise ratio (SNR), and rotational cycle/phase in Table 1. The raw data were reduced with LIBRE ESPRIT, the dedicated ESPaDOnS pipeline that produces one-dimensional Stokes I and V spectra from the raw ESPaDOnS images. The rotational cycles of TAP 4 and TAP 40 were, respectively, calculated from the following ephemerides:

$$\begin{aligned} \mathrm{BJD(d)} &= 2456611.83 + 0.482E \\ \mathrm{BJD(d)} &= 2456611.96 + 1.585E, \end{aligned} \quad (1)$$

where the start points were arbitrarily chosen. The rotational periods were taken from Grankin et al. (2008), but the value of TAP 40 has been fine-tuned for a better fit (see Section 4).

It is well known that (Zeeman) Doppler imaging needs to use well-sampled time series of profiles with high SNRs. Thus, least-squares deconvolution (LSD; Donati et al. 1997), which extracts a high-SNR average profile from thousands of photospheric lines, was applied to the observed Stokes I and V spectra. The stellar line lists used in the LSD process were obtained from a Kurucz model atmosphere (Kurucz 1993) with $T_{\rm eff} = 5250$ K and $\log g = 4.5$ for TAP 4 and the one with $T_{\rm eff} = 4750$ K and $\log g = 4.5$ for TAP 40. Lines in regions including telluric lines and strong chromospheric lines were removed from the lists. SNRs of the Stokes I and V LSD profiles are also listed in Table 1. SNRs of Stokes I profiles were derived from their continuum windows. Different to that of Stokes V profiles, the noise of Stokes I profiles is dominated by residual line blending generated by LSD (e.g. inaccurate line list), rather than the photon noise, and thus the performance of LSD for Stokes I spectra is smaller than that for Stokes V spectra (Donati et al. 1997).

Several stellar spectra of TAP 4 suffered from the moon light contamination. We thus performed the two-step process, proposed by Donati et al. (2016), to remove lunar contamination from the polluted spectra, with the help of the Doppler imaging. First, we performed Doppler imaging using the original Stokes I profiles excluding the polluted region, and then fitted the residuals with Gaussian profiles. Secondly, we subtracted the fitted Gaussian profiles from the affected profiles and then derived the final Doppler images.

Fig. 1 displays examples of LSD Stokes I and V profiles for TAP 4 and TAP 40. The Stokes I profile of the rapid rotator TAP 4 shows strong distortions and a flat bottom likely caused by a polar spot. The slower rotator TAP 40 shows clear Zeeman signatures in the Stokes V profile, but its unpolarized profile is nearly symmetric with respect to the line centre. Fig. 2 shows a dynamic spectrum of the phased Stokes I profiles of TAP 4, where each profile is subtracted from the averaged profile of all observations. The dynamic Stokes I profiles of TAP 4 show clear spot signatures moving from blue to red wavelengths. The dynamic Stokes V profiles (see Fig. 2) of TAP 4 and TAP 40 show similar

Table 1. Summary of observations.

UT Date	$\mathrm{BJD_{TT}}$ 2450000 +	SNR raw	SNR LSD-I	SNR LSD-V	Cycle/phase
TAP 4					
2013-11-15	6611.83559	103	888	2007	0.012
2013-11-15	6611.93441	89	860	1759	0.217
2013-11-15	6612.04650	84	819	1772	0.449
2013-11-16	6612.76210	101	878	1918	1.934
2013-11-16	6613.01104	97	860	1825	2.450
2013-11-17	6613.75459	97	894	1835	3.993
2013-11-17	6613.86670	108	947	2169	4.226
2013-11-17	6613.99974	100	904	1917	4.502
2013-11-17	6614.08710	96	887	1823	4.683
2013-11-18	6614.81879	93	874	1805	6.201
2013-11-19	6615.79046	101	899	1941	8.217
2013-11-19	6615.91156	98	888	1880	8.468
2013-11-19	6615.97844	97	867	1855	8.607
2013-11-19	6616.04393	97	875	1861	8.743
2013-11-20	6616.73490	84	810	1848	10.176
2013-11-20	6616.84261	96	858	1777	10.400
2013-11-20	6616.95424	90	854	1756	10.631
2013-11-20	6617.10569	78	607	2304	10.945
2013-11-23	6619.75070	91	866	1848	16.433
2013-11-23	6619.86170	88	863	1799	16.663
2013-11-23	6619.97877	114	967	2323	16.906
2013-11-23	6620.04474	111	959	2215	17.043
2013-11-24	6620.87867	102	909	1939	18.773
2013-11-25	6621.78141	107	904	2084	20.646
2013-11-25	6621.88841	113	933	2289	20.868
2013-11-25	6621.95597	110	934	2212	21.008
2013-11-25	6622.06311	107	913	2088	21.231
2013-11-26	6622.76619	106	896	2017	22.689
2013-11-26	6622.83456	110	926	2198	22.831
2013-11-26	6622.89830	113	936	2287	22.963
2013-11-26	6623.01087	99	892	1903	23.197
TAP 40					
2013-11-15	6611.96816	112	500	2062	0.005
2013-11-15	6612.09788	137	499	2543	0.087
2013-11-16	6612.92022	144	528	2759	0.606
2013-11-16	6613.08941	124	527	2295	0.713
2013-11-17	6613.83316	144	534	2766	1.182
2013-11-18	6614.89824	136	661	2712	1.854
2013-11-19	6615.86713	146	540	2813	2.465
2013-11-19	6616.01089	131	539	2433	2.556
2013-11-20	6616.91928	123	521	2278	3.129
2013-11-20	6617.03109	78	522	1633	3.199
2013-11-20	6617.07290	94	544	1619	3.226
2013-11-23	6619.82874	128	524	2397	4.965
2013-11-23	6620.01186	149	528	2870	5.080
2013-11-24	6620.91183	133	524	2502	5.648
2013-11-25	6621.92131	148	527	2850	6.285
2013-11-25	6622.09622	143	527	2693	6.395
2013-11-26	6622.80209	141	524	2625	6.840
2013-11-26	6622.93164	147	527	2800	6.922

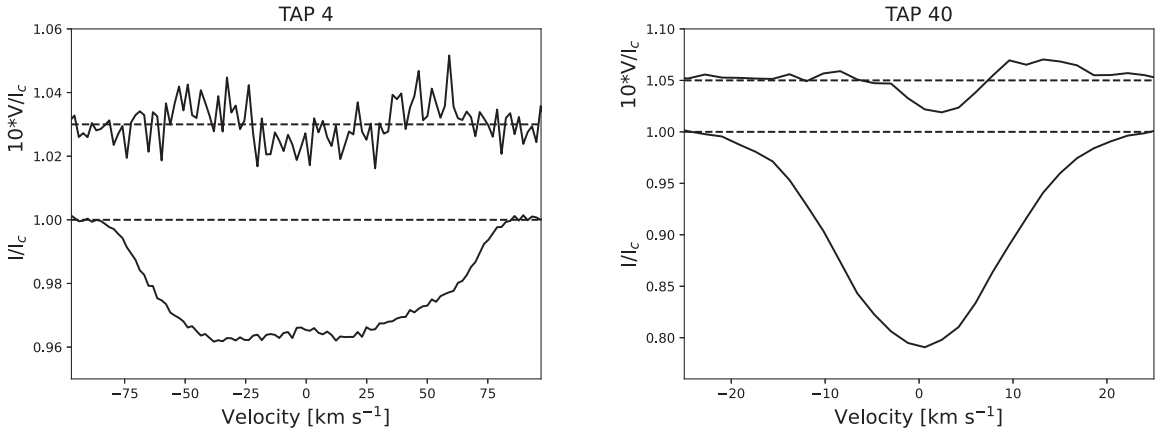

Figure 1. Examples of the Stokes I and V profiles of TAP 4 and TAP 40.

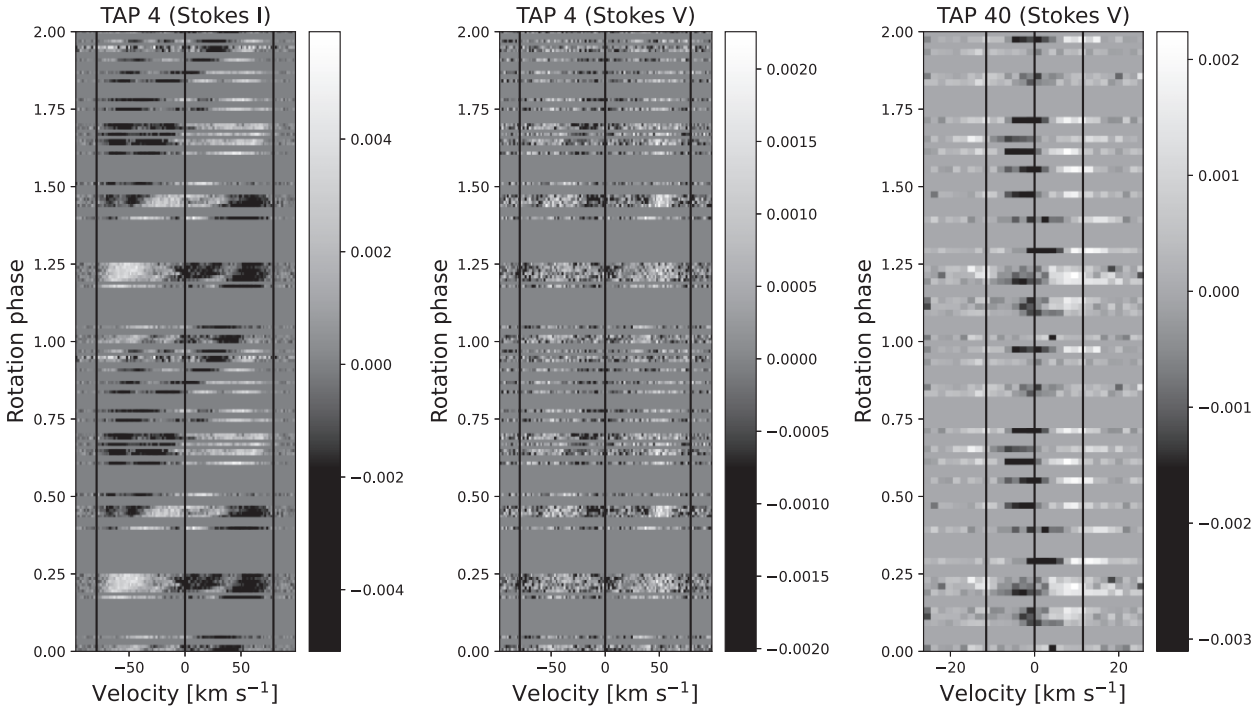

Figure 2. Dynamic spectra of Stokes I (left) and V (middle) profiles for TAP 4 and Stokes V profiles (right) of TAP 40, phased using the rotation period in equation (1). The average Stokes I profile was subtracted from Stokes I profile to emphasize spot signatures more clearly. The vertical lines represent $\pm v \sin i$ as well as the line centre in all panels.

symmetric features, likely related to toroidal fields (e.g. Lehmann & Donati 2022).

3 EVOLUTIONARY STATUS AND STELLAR PARAMETERS

The *Gaia* astrometric solution (Gaia Collaboration 2018, 2021, 2022) gives a parallax value of TAP 4, which is 6.878 ± 0.014 mas, corresponding to a distance of 145.4 ± 0.3 pc or a distance modulus of 5.813 ± 0.004. From long-term photometry, Grankin et al. (2008) observed a maximum V magnitude of 12.0 and thus the V magnitude of the unspotted star may be 11.8 ± 0.2 assuming a spot coverage of ∼20 per cent on the visible stellar surface. The effective temperature and logarithmic gravity of TAP 4 were derived using the spectral classification tool developed by Donati et al. (2012). The results are $T_{\rm eff}$ = 5190 ± 50 K and $\log g$ = 4.6 ± 0.2 in cgs units. The B–V index expected at this temperature is equal to 0.79 ± 0.02 (Pecaut & Mamajek 2013) and the observed averaged value is equal to 0.88 ± 0.05 (Grankin et al. 2008); thus, we derived that the visual extinction $A_{\rm V}$ is equal to 0.28 ± 0.15. The bolometric correction $\rm BC_V$ is equal to −0.27 ± 0.05 at this temperature (Pecaut & Mamajek 2013). Hence, the absolute bolometric magnitude $M_{\rm bol}$ is equal to 5.44 ± 0.27 and thus the luminosity of TAP 4 is $\log(L/{\rm L}_\odot) = -0.27 \pm 0.11$. Then, we derived a stellar mass of 0.95 ± 0.05 $\rm M_\odot$, a radius of 0.9 ± 0.1 $\rm R_\odot$, and a stellar age of about 47 Myr for TAP 4 from comparing the position of TAP 4 in the H–R diagram with the PMS evolutionary tracks of Siess, Dufour & Forestini (2000), assuming solar abundance with convective overshooting (see Fig. 3). Given the rotational period and $v \sin i$ of TAP 4, we can infer that $R_\star \sin i$

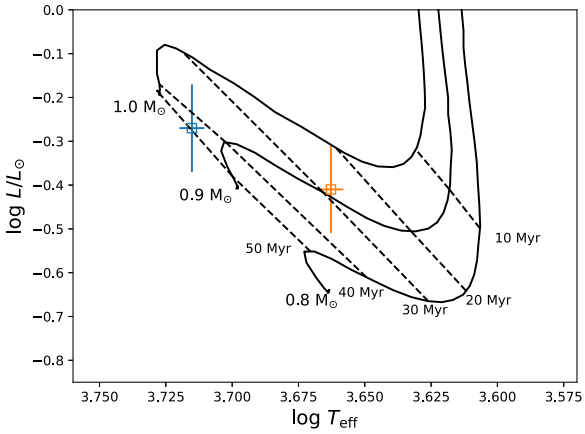

Figure 3. Estimated locations of TAP 4 (blue open square) and TAP 40 (orange open square) in the HR diagram. The PMS evolutionary tracks are taken from Siess et al. (2000), assuming solar metallicity with convective overshooting.

Table 2. Parameters of TAP 4 and TAP 40.

Parameters	TAP 4	TAP 40
$M_\star$ ($M_\odot$)	0.95 ± 0.05	0.91 ± 0.09
$R_\star$ ($R_\odot$)	0.9 ± 0.1	0.9 ± 0.1
Age (Myr)	∼47	∼28
log g (cgs)	4.6 ± 0.2	4.6 ± 0.2
$T_{\rm eff}$ (K)	5190 ± 50	4600 ± 50
$P_{\rm rot}$ (d)	0.482	1.585
$v \sin i$ (km s^{-1})	79 ± 0.5	12 ± 0.2
Inclination (°)	∼55	∼25
Distance (pc)[a]	145.4 ± 0.3	138.9 ± 0.3

[a] Gaia Collaboration (2018, 2021).

is equal to 0.75 ± 0.01 $R_\odot$ and thus the inclination of TAP 4 equals ∼55°.

From *Gaia*'s release, TAP 40's parallax value is 7.202 ± 0.016 mas (Gaia Collaboration 2021), translating to a distance of 138.9 ± 0.3 pc or a distance modulus of 5.714 ± 0.005. The maximum V magnitude of TAP 40 is 12.5 (Grankin et al. 2008) and the unspotted V magnitude may be 12.3 ± 0.2, assuming again a minimum spot coverage of 20 per cent on the visible stellar surface. From the observed spectra, we derived a $T_{\rm eff}$ of 4600 ± 50 K and a log g of 4.6 ± 0.2. The observed averaged B–V is 1.09 ± 0.02 (Grankin et al. 2008) and the expected one for this effective temperature is 1.17 (Pecaut & Mamajek 2013); thus, we can derive that the visual extinction $A_{\rm V}$ is equal to 0.25 ± 0.15. The bolometric correction is equal to -0.57 ± 0.05, and this results in an absolute bolometric magnitude of 5.77 ± 0.25. Thus, it can be derived that the luminosity of TAP 40 is $\log(L/L_\odot) = -0.41 \pm 0.1$. Then, we can infer that its stellar mass is 0.91 ± 0.09 $M_\odot$ and its radius is 0.9 ± 0.1 $R_\odot$. Compared with the evolutionary model of Siess et al. (2000), the age of TAP 40 is 28 Myr. The estimated $v \sin i$ of 12 ± 0.2 km s^{-1} implies that $R_\star \sin i$ is 0.35 ± 0.01 $R_\odot$ and thus the inclination of TAP 40 is about ∼25°. These adopted parameters of two stars are listed in Table 2.

4 ZEEMAN–DOPPLER IMAGING

We applied two imaging codes, ZDOTS (Hussain et al. 2000, 2002; Hussain, Jardine & Collier Cameron 2001) and ZDI (Donati et al. 2006, 2014), to the time series of Stokes I and V profiles to derive the surface brightness and magnetic field maps of TAP 4 and TAP 40. For the brightness map reconstruction, both codes allow cool and hot features to be recovered, as described by Donati et al. (2014). In the imaging process, we also derived the values of $v \sin i$ for the two stars and fine-tuned the rotational period for TAP 40, which are listed in Table 2.

Both imaging codes utilize the maximum entropy regularization (Skilling & Bryan 1984), but the definitions of the entropy are slightly different in the two codes (Hussain et al. 2000). Both codes implement a spherical harmonic decomposition of the magnetic field as described by Donati et al. (2006) but with $\beta_{l,m}$ replaced by $\alpha_{l,m} + \beta_{l,m}$, as follows (see Finociety & Donati 2022; Lehmann & Donati 2022):

$$B_r(\theta,\phi) = -\sum_{l,m} \alpha_{l,m} Y_{l,m}(\theta,\phi) \quad (2)$$

$$B_\theta(\theta,\phi) = -\sum_{l,m} [(\alpha_{l,m} + \beta_{l,m}) Z_{l,m}(\theta,\phi) + \gamma_{l,m} X_{l,m}(\theta,\phi)] \quad (3)$$

$$B_\phi(\theta,\phi) = -\sum_{l,m} [(\alpha_{l,m} + \beta_{l,m}) X_{l,m}(\theta,\phi) - \gamma_{l,m} Z_{l,m}(\theta,\phi)], \quad (4)$$

where

$$Y_{l,m} = c_{l,m} P_{l,m}(\cos\theta) e^{im\phi} \quad (5)$$

$$Z_{l,m} = \frac{c_{l,m}}{l+1} \frac{\partial P_{l,m}(\cos\theta)}{\partial\theta} e^{im\phi} \quad (6)$$

$$X_{l,m} = \frac{c_{l,m}}{l+1} \frac{P_{l,m}(\cos\theta)}{\sin\theta} im e^{im\phi} \quad (7)$$

$$c_{l,m} = \sqrt{\frac{2l+1}{4\pi} \frac{(l-m)!}{(l+m)!}}, \quad (8)$$

where $P_{l,m}(\cos\theta)$ is the associated Legendre polynomial. Therefore, the imaging codes recover the complex coefficients of spherical harmonic (SH) modes, $\alpha_{l,m}$, $\beta_{l,m}$, and $\gamma_{l,m}$, rather than the three components of the surface magnetic field for each independent pixel. This approach introduced a prior physical constraint on the reconstructed magnetic field map and allows one to easily derive the properties of poloidal and toroidal components of the surface magnetic field. Given $v \sin i$ of the two stars, we limited $l_{\rm max}$ to be 15 and 7 for TAP 4 and TAP 40, respectively. We also performed imaging with larger $l_{\rm max}$, but only obtained marginal changes.

4.1 Brightness and magnetic maps

We display the observed Stokes I and V profiles of TAP 4 as well as the maximum entropy fits derived by the two codes in Fig. 4, where the green lines in the Stokes I profiles represent the profiles before correction of the moon light contamination. For TAP 40, we find no clear modulated variations in its Stokes I profiles (see the left-hand panel in Fig. 5), which means that surface brightness inhomogeneities of TAP 40, if any, have a low contrast with respect to the photosphere. The observed V profiles of TAP 40 and the corresponding fits to them are shown in the right-hand panel of Fig. 5. As can be seen, the two codes give very consistent solutions to the observed profiles of TAP 4 and TAP 40. The fits correspond to the reduced chi-square χ^2_r of 1 for TAP 4 and 1.2 for TAP 40 by both codes. The brightness and magnetic maps of TAP 4 were derived separately from Stokes I and V profiles.

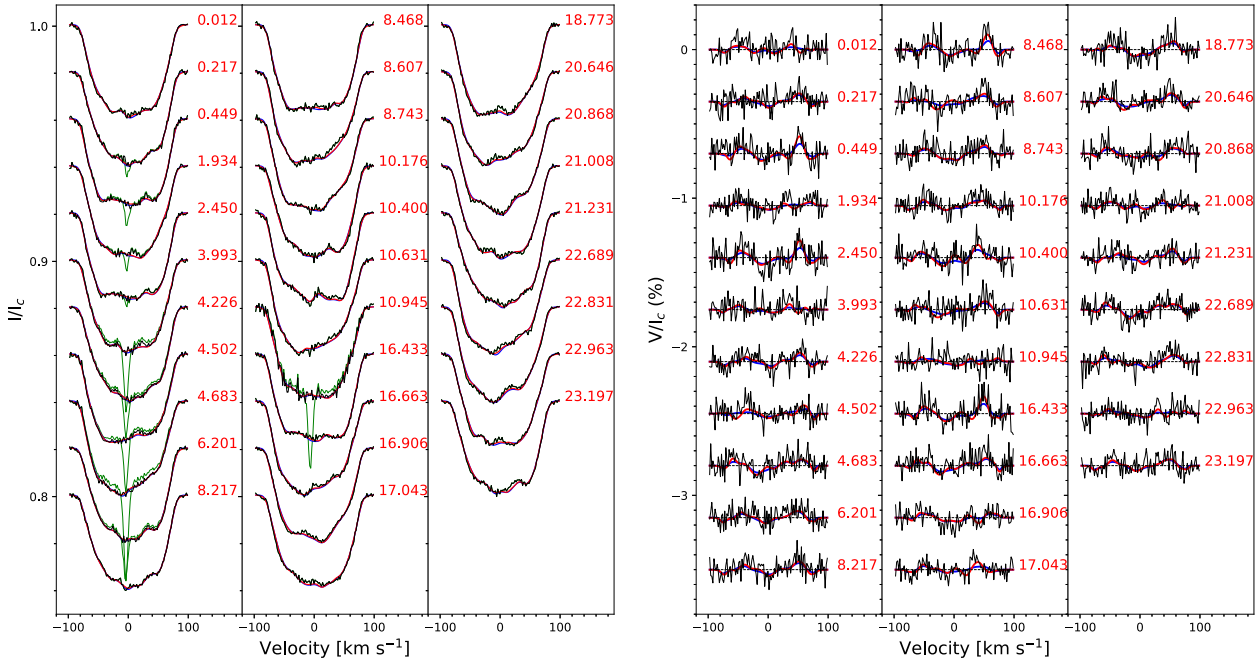

Figure 4. Maximum entropy fits (blue lines for ZDOTS and red lines for ZDI) to the observed (black lines) Stokes I (left) and Stokes V (right) LSD profiles of TAP 4. The lunar contaminations are shown in green.

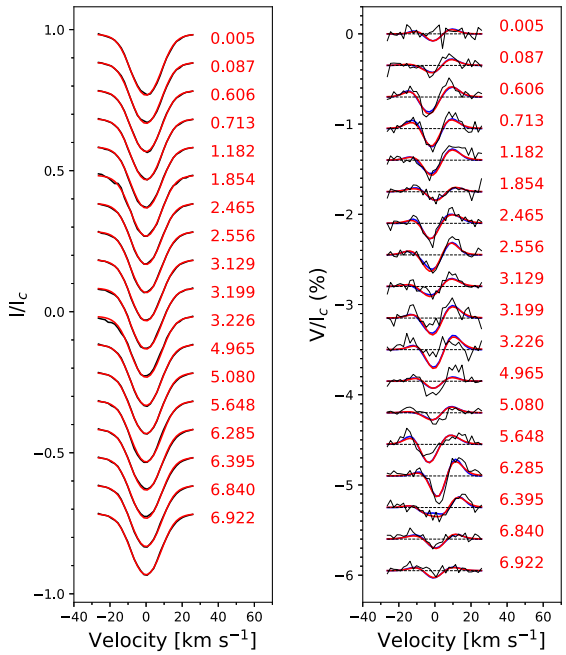

Figure 5. Left-hand panel shows the observed Stokes I profiles (black) and the immaculate profiles (red) for TAP 40. Right-hand panel shows the maximum entropy fits derived by ZDOTS (blue) and ZDI (red) to the Stokes V profiles (black) of TAP 40.

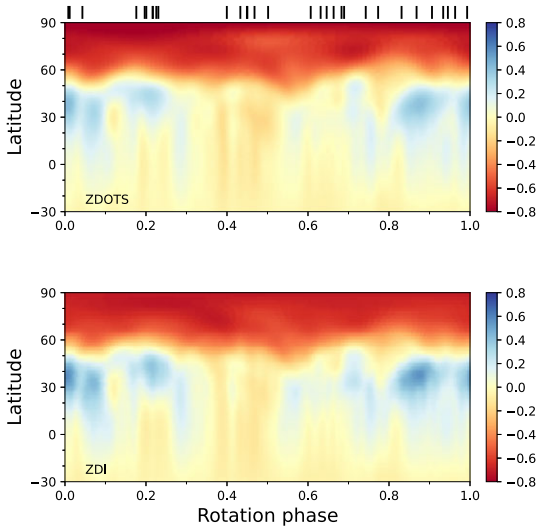

Figure 6. Images of the logarithmic surface brightness relative to the photosphere of TAP 4, produced by ZDOTS (top) and ZDI (bottom). For convenient comparison, both are rectangular and along the same longitudinal direction.

The brightness map reconstructions of TAP 4 derived by ZDOTS and ZDI are shown in Fig. 6. Both images show the logarithmic brightness relative to the photosphere. The surface features recovered by the two codes are nearly identical to each other.

The most prominent feature on the surface brightness map of TAP 4 is the large, cool polar spot with some appendages extending to low latitudes. This polar spot is related to the flat bottom of the observed Stokes I profiles (Fig. 4). In addition to the cool spots, TAP 4 also exhibits warm features at intermediate latitudes. The warm features shape a ring structure at a latitude of about 40°. The coverage of the cool spots on TAP 4 is 7 per cent and the value of the warm spots is 5 per cent. However, the coverage derived from the reconstructed image should be underestimated since Doppler imaging is only sensitive to the large-scale, inhomogeneous features. The small-sized spots and symmetric structures on the stellar surface cannot be recovered by the Doppler imaging.

The magnetic maps of TAP 4 and TAP 40 derived by ZDOTS and ZDI are also in good agreement, which are displayed in Figs 7

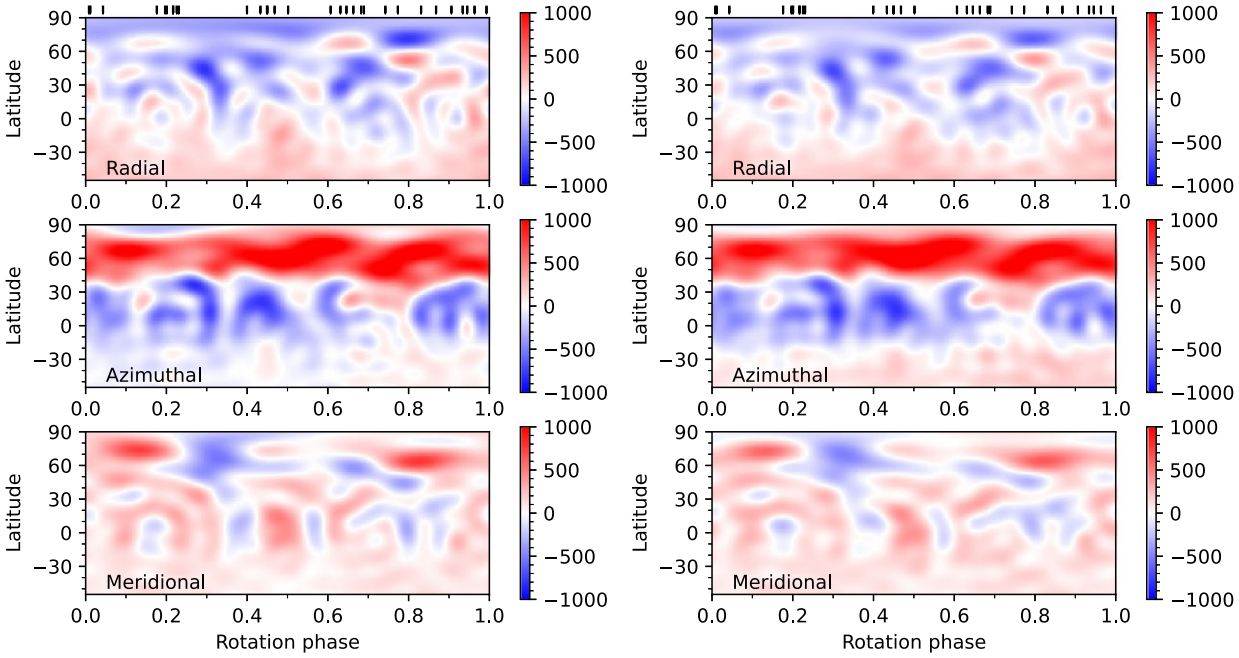

Figure 7. Large-scale magnetic field maps of TAP 4 derived by ZDOTS (left) and ZDI (right).

and 8, respectively. The properties of the magnetic field of TAP 4 and TAP 40 derived from the spherical harmonic coefficients obtained by the two codes are listed in Table 3. The reconstructed magnetic maps show a complex large-scale magnetic structure on the surface of TAP 4. The poloidal and toroidal components enclose 40 and 60 per cent of the total magnetic energy, respectively. The toroidal field of TAP 4 is dominated by the axisymmetric component, which is related to the strong positive ring structure of the azimuthal field as shown in the middle panel of Fig. 7. The radial field on TAP 4 is mainly dominated by the complex, non-axisymmetric, negative poloidal field. The large-scale dipole field of TAP 4 is tilted at $\sim 22^\circ$ with respect to the rotation axis.

TAP 40 hosts a relatively simple large-scale magnetic field. The toroidal field is again the dominant component, enclosing more than 60 per cent of the total magnetic energy. This toroidal field shows up as a ring-like pattern in the azimuthal field map of TAP 40 in the middle panel of Fig. 8. The dipole field of TAP 40 is tilted at $\sim 42^\circ$ with respect to the rotation axis.

Based on the potential field source surface model presented by Jardine et al. (2013), we derived the extrapolation of the coronal magnetic field from the radial component of the reconstructed magnetic fields of TAP 4 and TAP 40. The source surfaces, where all magnetic field lines become radial, were set to 3 $R_\star$ for TAP 4 and 6 $R_\star$ for TAP 40, close to the corotation radii of these two stars, respectively. The extrapolation results are shown in Fig. 9.

4.2 Surface differential rotation

Doppler imaging is also commonly used for the determination of surface differential rotation. The estimate can be achieved either by the cross-correlation of two reconstructed maps observed at close epochs or by looking for the differential rotation parameters that best fit the observed data (Donati & Collier Cameron 1997; Donati et al. 2000; Petit, Donati & Collier Cameron 2002). The shear method takes the surface differential rotation into account as part of the imaging process, which requires longer observations for differential rotation to be detectable with Doppler imaging.

The observations of TAP 4 span more than 23 rotation cycles, which makes the data set well suited to estimate surface differential rotation. We thus applied the Doppler imaging code to the Stokes I profiles of TAP 4, with the assumption of a simple solar-like differential rotation law described by equation

$$\Omega(\theta) = \Omega_{\rm eq} - {\rm d}\Omega \sin^2\theta, \tag{9}$$

where $\Omega(\theta)$ is the rotation rate at latitude θ and $\Omega_{\rm eq}$ is the rotation rate at the stellar equator and dΩ is the difference between rotation rates at the stellar equator and the pole. We derived Doppler images for various differential rotation parameter pairs of $\Omega_{\rm eq}$ and dΩ at constant information content and recorded the resulting χ_r^2. Then, we fitted a paraboloid to the surface of χ_r^2 distribution to find the parameter pair that leads to the minimum χ_r^2 (Donati, Collier Cameron & Petit 2003).

We show the contour plot of χ_r^2 versus the differential rotation parameter pairs derived from the brightness and magnetic images of TAP 4 in Fig. 10. By fitting Stokes I profiles, we found a surface differential rotation rate of ${\rm d}\Omega = 0.105 \pm 0.007$ rad d^{-1} and an equatorial rotation rate of $\Omega_{\rm eq} = 13.059 \pm 0.002$ rad d^{-1} for TAP 4. From Stokes V profiles, we derived the surface shear rate of ${\rm d}\Omega = 0.065 \pm 0.014$ rad d^{-1} and an equatorial rotation rate of $\Omega_{\rm eq} = 13.033 \pm 0.007$ rad d^{-1}.

4.3 Filtering the activity jitter

Young stars often exhibit high level of magnetic activity, which results in severe problems when trying to detect orbiting exoplanets through RV measurements. Magnetic activity can distort stellar spectral line profiles severely and thus induce large jitters in the RV curves of the order of a few km s^{-1} (Donati et al. 2014; Hébrard et al. 2014). As a comparison, the RV amplitude of a low-mass star caused by the presence of a Jupiter-mass close-in planet is of about 0.1 km s^{-1} (e.g. Donati et al. 2017).

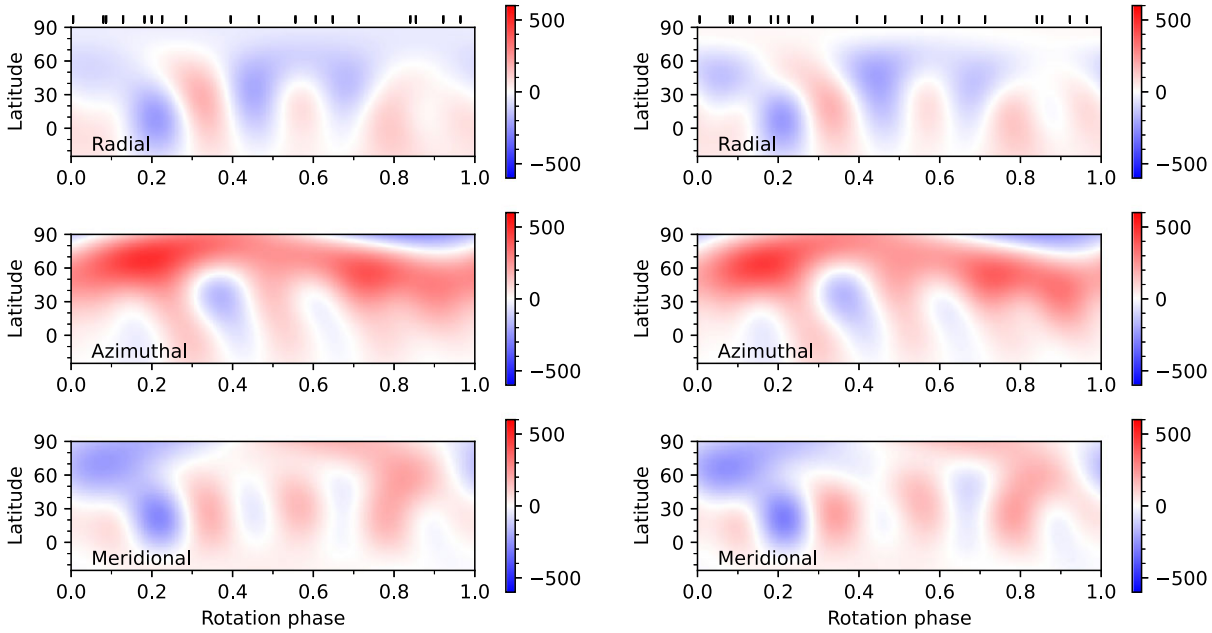

Figure 8. Same as Fig. 7, but for TAP 40.

Table 3. Properties of the magnetic fields of TAP 4 and TAP 40 derived by the two codes.

Parameters	ZDOTS	ZDI
TAP 4		
$<B>$ (G)	449	447
Poloidal (percentage total)	40	36
Dipole (percentage poloidal)	37	42
Dipole tilt (°)	22	22
Dipole phase	0.51	0.49
Poloidal axisymmetric (percentage poloidal)	44	50
Toroidal (percentage total)	60	64
Toroidal axisymmetric (percentage toroidal)	90	92
TAP 40		
$<B>$ (G)	168	163
Poloidal (percentage total)	34	36
Dipole (percentage poloidal)	18	14
Dipole tilt (°)	43	42
Dipole phase	0.34	0.33
Poloidal axisymmetric (percentage poloidal)	15	14
Toroidal (percentage total)	66	64
Toroidal axisymmetric (percentage toroidal)	71	66

Another goal of the MaTYSSE programme is to detect close-in giant planets orbiting young active stars, which will provide important constraints for planet formation models. The technique proposed by Donati et al. (2014) takes advantage of the tomographic modelling to filter the activity jitter in RV curves. Given the reconstructed brightness map of an active star, one can predict the RV jitter induced by surface activity and filter them out from the raw RV measurements so that the detection of small-amplitude RV variation caused by a close-in giant planet becomes detectable. So far, hJs orbiting two young active stars, V830 Tau (Donati et al. 2016) and TAP 26 (Yu et al. 2017), have been detected within the MaTYSSE programme.

We performed the filtering process on the RV measurements of TAP 4, using the brightness map derived in Section 4.1. Due to the large gap within the observing run for TAP 4, we split the original data set of TAP 4 into two subsets to reduce the rms caused by the evolution of the surface brightness map of TAP 4. The first subset spans rotation cycles 0–11 and the other one spans rotation cycles 16–24. The amplitude of the unfiltered RVs of TAP 4 is about 2 km s^{-1}, where the RVs of TAP 4 are derived from the first-order moment of the observed Stokes I profiles, rather than by a Gaussian fit due to the high v sin i and the distorted profile shapes. The RVs induced by the surface activity are shown in Fig. 11 as orange lines. The rms dispersion of the residuals is 0.20 km s^{-1}, which is much larger than the intrinsic RV precision of ESPaDOnS of 0.03 km s^{-1} (Donati et al. 2014). The high v sin i of TAP 4 strongly limits the accuracy of the filtering process. The mean 1σ error of the RV measurements is 0.19 km s^{-1} for TAP 4 and the filtered RVs are not statistically different from the zero, which means that TAP 4 is unlikely to host a close-in planet.

5 DISCUSSION AND CONCLUSIONS

In this work, we presented a Zeeman–Doppler imaging study of two young active stars, TAP 4 and TAP 40, based on new high-resolution spectropolarimetric data collected with ESPaDOnS at CFHT in November 2013, within the MaTYSSE large programme.

The analysis on the new high-resolution spectroscopic data shows that TAP 4 has a $T_{\rm eff}$ of 5190 ± 50 K and a log g of 4.6 ± 0.2 and TAP 40 has a $T_{\rm eff}$ of 4600 ± 50 K and a log g of 4.6 ± 0.2. TAP 4 is a rapidly rotating star with a v sin i of 79 ± 0.5 km s^{-1}, whereas TAP 40 is a relatively slower rotator with a v sin i of 12 ± 0.2 km s^{-1}. Based on the parallax values from the *Gaia* astrometric solution (Gaia Collaboration 2018) and the photometric data of Grankin et al. (2008), we obtain the locations of these two stars on the HR diagram (Fig. 3). Combining with the evolutionary tracks of Siess et al. (2000), we find that TAP 4 has a stellar mass of 0.95 ± 0.05 M$_\odot$ and a radius

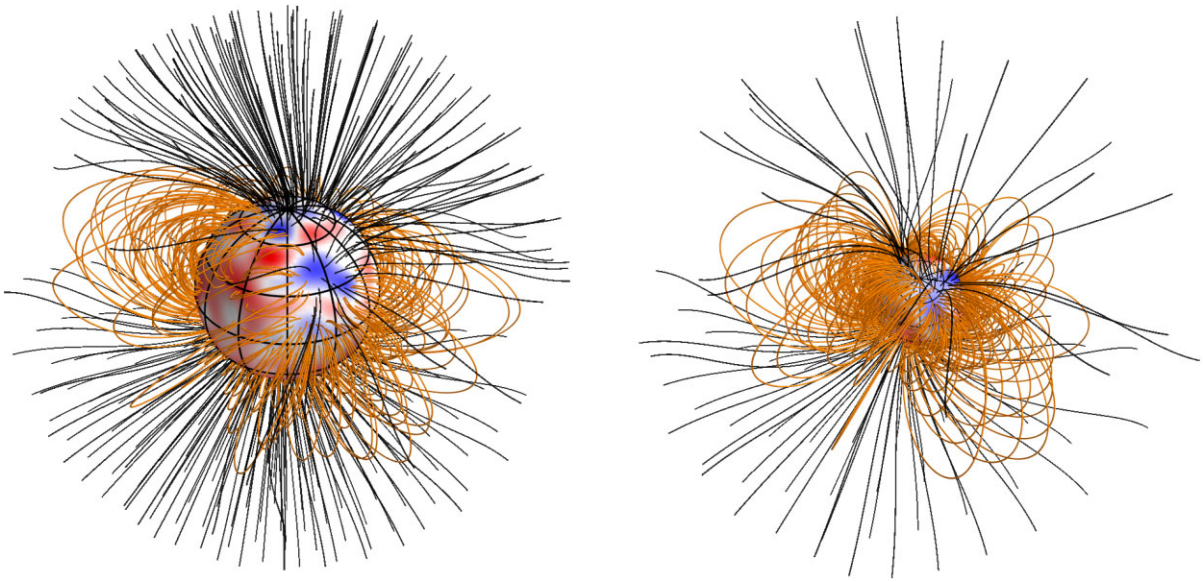

Figure 9. Potential field extrapolations for TAP 4 and TAP 40, as viewed by an Earth-based observer, at phase 0.75. The orange lines represent the closed magnetic lines and the black lines denote the open magnetic lines. The source surfaces are set to 3 $R_\star$ for TAP 4 and 6 $R_\star$ for TAP 40, close to the corotation radii of the two stars.

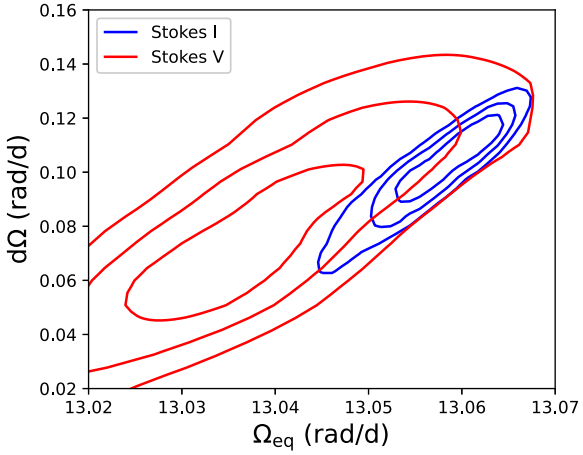

Figure 10. Contour plot of χ^2_r versus Ω_{eq} and dΩ pairs derived from the tomographic modelling on the Stokes I (blue) and V (red) profiles of TAP 4. The lines denote 1σ, 2σ, and 3σ boundaries.

of $0.9 \pm 0.1\,R_\odot$ and TAP 40 has a mass of $0.91 \pm 0.09\,M_\odot$ and a radius of $0.9 \pm 0.1\,R_\odot$. The ages of TAP 4 and TAP 40 are 47 and 28 Myr, respectively. Therefore, TAP 4 is probably at the late stage of wTTS phase and very close to the zero-age main sequence (ZAMS).

We applied two Zeeman–Doppler imaging codes to the time series of Stokes I and V profiles to reconstruct their surface brightness and magnetic field images. However, the time series of Stokes I profiles of TAP 40 show minimal variations, meaning that brightness features have a low contrast with respect to the photosphere at the surface of this star. The reconstructed surface brightness and magnetic field maps of both stars derived by the two different codes are in very good agreement with each other.

The brightness map of TAP 4 shows a pronounced, cool polar spot with some dark appendages extending to lower latitudes. The cool spot is not symmetric with respect to the rotation pole. In addition, the presence of warm spots is found at a latitude of 40° on TAP 4. Considering the high v sin i and the short rotation period of TAP 4, the polar spot is expected by the magnetic flux emergence and transport models (e.g. Işık, Schüssler & Solanki 2007; Işık, Schmitt & Schüssler 2011; Işık et al. 2018). Similar polar features are commonly detected on the rapidly rotating young stars, e.g. TWA6 (Hill et al. 2019), V530 Persei (Cang et al. 2020), and V471 Tau (Zaire, Donati & Klein 2021). Meanwhile, similar intermediate-latitude warm features are found on wTTSs with different parameters, e.g. LkCa 4 (Donati et al. 2014), V830 Tau (Donati et al. 2016), and TAP 26 (Yu et al. 2019). We may infer that the configuration of the surface brightness map of TAP 4 is very common among wTTSs.

TAP 40 shows very weak variations in its Stokes I profiles, which is consistent with the photometric results of Grankin et al. (2008). In their analysis, TAP 40 only exhibited a mean V-band photometric amplitude of 0.109 mag, though their photometric observations were at different epochs. The small variations in the unpolarized profiles of TAP 40 are likely due to the low inclination.

The large-scale magnetic field of TAP 4 is more complex than that on TAP 40, which may be partly due to the lower v sin i of TAP 40 resulting in the lower resolution of its Zeeman–Doppler image. However, the most prominent features of the magnetic fields of these two stars are similar, which is a strong ring pattern of the azimuthal field seen on both surfaces of TAP 4 and TAP 40, as shown in Figs 7 and 8. Both of the magnetic reconstructions of TAP 4 and TAP 40 indicate predominant toroidal fields enclosing about 60 per cent of the total magnetic field energy. The dominance of the toroidal field is consistent with the inference of Petit et al. (2008), who showed that the rapid rotators with short periods are more likely to host dominant toroidal components. The ratio of the poloidal and toroidal fields is dependent on the Rossby number (Donati & Landstreet 2009).

Thanks to the long duration of the observing run for TAP 4, which covers more than 23 rotation cycles, it allows us to derive the surface differential rotation rate of TAP 4. Under the simple assumption of a solar-like differential rotation law, we obtain a surface shear of 0.105 ± 0.007 rad d^{-1} from Stokes I profiles and 0.065 ± 0.014 rad d^{-1} from Stokes V profiles. In literature, the solar-like surface differential rotation is detected on various PMS to ZAMS stars, e.g. V471 Tau (Hussain et al. 2006; Zaire et al. 2021, 2022) and HD

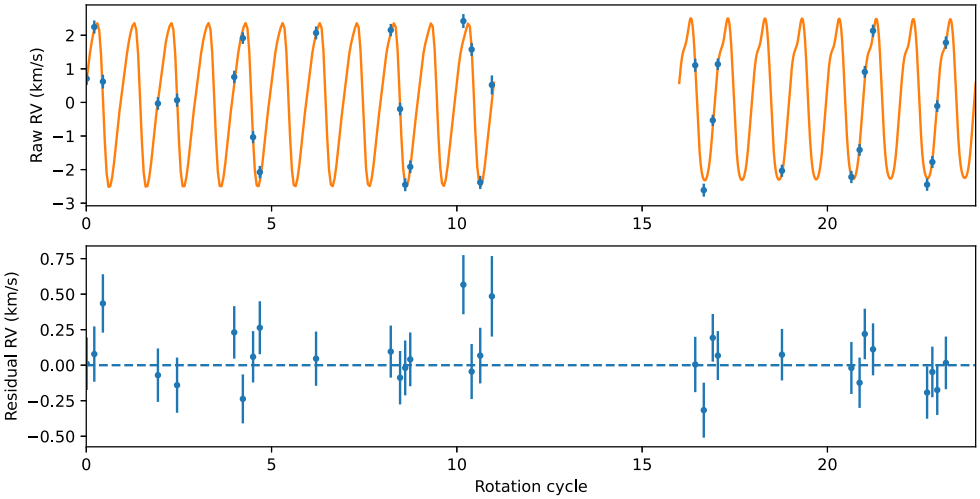

Figure 11. Filtering the RV jitters induced by the magnetic activity for TAP 4.

155 555 (Dunstone et al. 2008). The rapidly rotating ZAMS star AB Dor even shows variations in the surface differential rotation with years (Donati et al. 2003; Jeffers, Donati & Collier Cameron 2007). The value of the surface shear we derived for TAP 4 is relatively common among the wTTSs sample of the MaTYSSE programme. Differential rotation is one of the key ingredients of stellar dynamos, which amplify and sustain the stellar magnetic fields. Estimates of surface differential rotation on young active stars bring constraints on stellar dynamo models for stars at early evolutionary stages.

The tomographic modelling of TAP 4 is also used for filtering the activity-induced RV jitter to search for the potential close-in massive exoplanet. The rms of the filtered RVs we achieve is 0.2 km s^{-1} from an initial dispersion of raw RVs of 1.7 km s^{-1}. The dispersion is higher than that for other wTTSs in the MaTYSSE programme, e.g. LkCa 4 (Donati et al. 2014), but similar to that for TWA 6 (Hill et al. 2019). The larger uncertainty is due to the relatively high v sin i of TAP 4. We do not find obvious deviations of the filtered RVs of TAP 4, and the filtered RV curve does not show any significant periodic signal. RV simulations can be used to derive the detection limit on the mass of potential exoplanets (Yu et al. 2019; Finociety et al. 2021; Nicholson et al. 2021). We simulated the RV signatures from planets with various masses at a distance of 0.1 au assuming a circular orbit and found that an exoplanet more massive than $\sim 3.5 M_{\rm Jup}$ orbiting TAP 4 would have been detectable at a 3σ level with our data. With a false alarm probability smaller than 1 per cent, we can thus conclude that no close-in planet more massive than $3.5 M_{\rm Jup}$ orbits TAP 4 at a distance of about 0.1 au.

ACKNOWLEDGEMENTS

This paper is based on observations obtained at the CFHT, operated by the National Research Council of Canada, the Institut National des Sciences de l'Univers of the Centre National de la Recherche Scientifique (INSU/CNRS) of France, and the University of Hawaii. We would like to thank the anonymous referee for taking the time to review this manuscript. This study was supported by the National Natural Science Foundation of China under grant numbers 10373023, 10773027, U1531121, 11603068, and 11903074. We acknowledge the science research grant from the China Manned Space Project with NO. CMS-CSST-2021-B07. JFD acknowledges funding from the European Research Council (ERC) under the H2020 research & innovation programme (grant agreement #740651 New-Worlds). This work has made use of data from the European Space Agency (ESA) mission Gaia (https://www.cosmos.esa.int/gaia), processed by the Gaia Data Processing and Analysis Consortium (DPAC, https://www.cosmos.esa.int/web/gaia/dpac/consortium). Funding for the DPAC has been provided by national institutions, in particular the institutions participating in the Gaia Multilateral Agreement.

DATA AVAILABILITY

The raw data used in this work from the CFHT can be obtained at the CADC (https://www.cadc-ccda.hia-iha.nrc-cnrc.gc.ca/en/cfht/).

REFERENCES

Basri G., Martin E. L., Bertout C., 1991, A&A, 252, 625
Cang T. Q. et al., 2020, A&A, 643, A39
Donati J. F. et al., 2016, Nature, 534, 662
Donati J.-F. et al., 2006, MNRAS, 370, 629
Donati J.-F. et al., 2012, MNRAS, 425, 2948
Donati J.-F. et al., 2014, MNRAS, 444, 3220
Donati J.-F. et al., 2015, MNRAS, 453, 3706
Donati J.-F. et al., 2017, MNRAS, 465, 3343
Donati J.-F. et al., 2019, MNRAS, 483, L1
Donati J.-F., Collier Cameron A., 1997, MNRAS, 291, 1
Donati J.-F., Collier Cameron A., Petit P., 2003, MNRAS, 345, 1187
Donati J.-F., Landstreet J. D., 2009, ARA&A, 47, 333
Donati J.-F., Mengel M., Carter B. D., Marsden S., Collier Cameron A., Wichmann R., 2000, MNRAS, 316, 699
Donati J.-F., Semel M., Carter B. D., Rees D. E., Collier Cameron A., 1997, MNRAS, 291, 658
Dunstone N. J., Hussain G. A. J., Collier Cameron A., Marsden S. C., Jardine M., Stempels H. C., Ramirez Velez J. C., Donati J.-F., 2008, MNRAS, 387, 481
Finociety B. et al., 2021, MNRAS, 508, 3427
Finociety B., Donati J.-F., 2022, MNRAS, 516, 5887
Gaia Collaboration, 2018, A&A, 616, A1
Gaia Collaboration, 2021, A&A, 649, A1
Gaia Collaboration, 2022, preprint (arXiv:2208.00211)
Grankin K. N., 2013, Astron. Lett., 39, 251
Grankin K. N., Bouvier J., Herbst W., Melnikov S. Y., 2008, A&A, 479, 827
Hackman T., Lehtinen J., Rosén L., Kochukhov O., Käpylä M. J., 2016, A&A, 587, A28

Hébrard É. M., Donati J.-F., Delfosse X., Morin J., Boisse I., Moutou C., Hébrard G., 2014, MNRAS, 443, 2599
Hill C. A., Carmona A., Donati J.-F., Hussain G. A. J., Gregory S. G., Alencar S. H. P., Bouvier J., MaTYSSE Collaboration, 2017, MNRAS, 472, 1716
Hill C. A., Folsom C. P., Donati J.-F., Herczeg G. J., Hussain G. A. J., Alencar S. H. P., Gregory S. G., MaTYSSE Collaboration, 2019, MNRAS, 484, 5810
Hussain G. A. J. et al., 2016, A&A, 585, A77
Hussain G. A. J., Allende Prieto C., Saar S. H., Still M., 2006, MNRAS, 367, 1699
Hussain G. A. J., Donati J.-F., Collier Cameron A., Barnes J. R., 2000, MNRAS, 318, 961
Hussain G. A. J., Jardine M., Collier Cameron A., 2001, MNRAS, 322, 681
Hussain G. A. J., van Ballegooijen A. A., Jardine M., Collier Cameron A., 2002, ApJ, 575, 1078
Işık E., Schmitt D., Schüssler M., 2011, A&A, 528, A135
Işık E., Schüssler M., Solanki S. K., 2007, A&A, 464, 1049
Işık E., Solanki S. K., Krivova N. A., Shapiro A. I., 2018, A&A, 620, A177
Jardine M., Vidotto A. A., van Ballegooijen A., Donati J.-F., Morin J., Fares R., Gombosi T. I., 2013, MNRAS, 431, 528
Jeffers S. V., Donati J.-F., Collier Cameron A., 2007, MNRAS, 375, 567
Kurucz R. L., 1993, Kurucz CD-ROM. Smithsonian Astrophys. Obs., Cambridge, MA
Lehmann L. T., Donati J.-F., 2022, MNRAS, 514, 2333
Nicholson B. A., Hussain G., Donati J.-F., Wright D., Folsom C. P., Wittenmyer R., Okumura J., Carter B. D., 2021, MNRAS, 504, 2461
Pecaut M. J., Mamajek E. E., 2013, ApJS, 208, 9
Petit P. et al., 2008, MNRAS, 388, 80
Petit P., Donati J.-F., Collier Cameron A., 2002, MNRAS, 334, 374
Rosén L., Kochukhov O., Hackman T., Lehtinen J., 2016, A&A, 593, A35
Semel M., 1989, A&A, 225, 456
Siess L., Dufour E., Forestini M., 2000, A&A, 358, 593
Skilling J., Bryan R. K., 1984, MNRAS, 211, 111
Yu L. et al., 2017, MNRAS, 467, 1342
Yu L. et al., 2019, MNRAS, 489, 5556
Zaire B., Donati J.-F., Klein B., 2021, MNRAS, 504, 1969
Zaire B., Donati J.-F., Klein B., 2022, MNRAS, 513, 2893

This paper has been typeset from a TEX/LATEX file prepared by the author.